Dynamics of gas bubbles in fiber suspensions

Ajinkya Pawar, Gilles Ausias, Julien Férec

Version of Record: https://www.sciencedirect.com/science/article/pii/S0301932221002512
Manuscript_e2090c035e64af3e1d79e70f1f29ea75

International Journal of Multiphase Flow (2021) 1–13

Journal Logo

Dynamics of gas bubbles in fiber suspensions

Ajinkya Pawar[a], Gilles Ausias[a], Julien Férec[a,*]

[a] *Univ. Bretagne Sud, UMR CNRS 6027, IRDL, F-56100 Lorient, France*

Abstract

The collapse/expansion of a spherical bubble in a Newtonian fluid filled with non-Brownian fibers is numerically investigated. An experimental test was conducted to observe that the spherical geometry of the bubble is maintained during the foaming process. The constitutive equation for the fiber suspension arises from the slender body theory and is coupled with an evolution equation describing the fiber dynamics. First solutions are proposed using steady fiber orientation distributions and the effect of the coupling coefficient on the bubble radius is examined. Later the condition of fixed microstructure is relaxed and the fibers are able to orient along with bubble expansion. Starting with a 3D random orientation, fibers close to the interface orient randomly in planes orthogonal to the radial direction, depending on the level of fiber-fiber interactions. For interaction coefficients encountered in polymer processing, fibers exhibit a closely 2D random planar orientation in a plane tangent to the cavity surface which prevents the bubble to collapse, as observed experimentally.

Keywords: Single bubble dynamics; Fiber suspensions; Theoretical modeling; Fiber orientation.

1. Introduction

The demand for lighter and stronger materials has generated tremendous interest in the development of polymeric foams. Polymeric foams are composites consisting of at least two phases, fabricated using blowing agents to attain desired cellular morphology. They have properties such as high strength to weight ratio, excellent insulation, high fatigue life, great impact strength and toughness [1] along with cost-effective manufacturing process which has made it lucrative in the packaging, automobile, marine, and sporting equipment industries. To further enhance desired properties in foams various methods such as blending of polymers, addition of reinforcements, and innovative fabrication technique [2] have been tested by many researchers. Yang et al. [3] investigated a hybrid polypropylene (PP) foam by varying mass fraction of short glass fiber (SGF) content. The average cell diameter was reduced along with better homogeneous dispersion by addition SGF, also the impact and flexural strength were found to improve by increasing the SGF content up to 20%. Similarly, Wang and Ying [4] investigated the cellular structure of PP foams manufactured by batch process using carbon fiber (CF) reinforcement as a nucleating agent and supercritical carbon dioxide as a blowing agent to study the effects of pressure saturation, depressurisation and CF content on the cell morphology. Xiao and Huang [5] fabricated a high-density nanostructured thermoplastic polyurethane (TPU) foams by increasing the reduced graphene oxide volume fraction from 0.25 to 0.75 which also improved the cell diameter distribution. Gayaneh et al. [6] tested the piezoelectric properties of TPU foams manufactured using thermally expandable microspheres as a foaming agent reinforced with lead zirconate titanate (PZT). The dielectric permittivity was found to increase with increasing the PZT content, along with a decrease in cell size with increasing PZT content.

*Corresponding author
Email address: julien.ferec@univ-ubs.fr (Julien Férec)

A lot of work has been devoted to investigate the problem of bubble growth and cavitation because of its involvement in many applications and process [7]. Rayleigh [8] was the pioneer to explore and solve the problem of the collapse of an empty cavity in a large mass of incompressible media. This work was then extended by Plesset and coworkers [9, 10] to include the effects of surface tension and fluid viscosity. Street et al. [11] considered a single bubble growth in a power-law fluid and the diffusion of the blowing agent. When dealing with viscoelastic surrounding fluids, Arefmanesh and Advani [12, 13] used an upper convected Maxwell (UCM) model to describe the nonisothermal bubble growth in polymeric foams. Allen and Roy [14] investigated the nonlinear oscillations of spherical acoustically forced gas bubbles in linear viscoelastic fluids which obey to the linear Maxwell and Jeffreys models. In contrast to their previous work, Allen and Roy [15] examined the large-amplitude excursions of a bubble in nonlinear viscoelastic media modeled by a UCM constitutive equation. Recently, Kawaguchi and his coworkers [16, 17] proposed a complete mathematical model for thermally expandable microcapsules growth surrounded by polymers. Their approach considers mass and transfer equations including diffusion, as well as the viscoelastic properties of polymeric microballoon using the UCM model.

Over the past decades, researchers developed numerical strategies to perform fiber orientation predictions for flows inside complex geometries with addressing the coupling between the flow field and the fiber orientation distribution [18, 19, 20]. To the best of our knowledge, the problem of bubble growth and cavitation in a fiber suspension was only been investigated by Evans [21, 22]. The reinforcement quantity has a clear effect on the cell size in the polymeric foams, and it is well known that the fiber orientation affects the mechanical properties in a composite. There is very little study done on the effect of fiber orientation on the expansion or collapse of the cells in polymeric foams. Therefore, this paper aims to fill the latter gap.

This paper presents a numerical model that captures a bubble dynamics in a fiber suspension as well as the kinetics of fiber orientation for collapsing/expanding the cavity. In Section 2 some experimental observations are presented showing the SEM characterisation for a fiber filled system with unexpanded and expanded microspheres. Section 3 describes the theoretical modeling, in which the extra stress resulting from the fiber hydrodynamics is considered and, Section 4 examines the model predictions for bubble collapsing and expanding. This paper focuses particularly on the effect of the fiber orientation distribution close to the bubble cavity. Finally,a short conclusion and perspectives end the paper.

2. Experimental observation

2.1. Raw Materials

The polymer matrix used for preparing the fiber-reinforced foam samples were polypropylene heterophasic copolymer PPC 10642 supplied by Total and glass fiber reinforced polypropylene ISPLEN PG370AS Supplied by Repsol containing 30wt% glass fiber. The most crucial component for manufacturing of foams is the blowing agent which creates the foam. Classically blowing agents such as hollow spheres, CO2, CFC's, etc, are used in manufacturing of foams. In this paper the foam was manufactured using thermally expandable microspheres (TEM) as the blowing agent. TEM's consists of polymeric shell encapsulating an aliphatic hydrocarbon, which on subjecting to heat, soften the thermoplastic shell, and as the gas inside the shell expands the TEM expand. This results in a dramatic volumetric increase of the microsphere size which on a larger scale produces the foaming effect. The TEM's were produced and supplied by Kureha GmbH under the trade name Kureha microspheres. The tests were conducted using S grade of Kureha microspheres, available in masterbatch pellets form know as MB-S6LB S2640 which constitute 60 wt% S2640 grade TEM's and 40 wt% polyethylene acting as a polymer carrier for the TEM's. The S2640 grade TEM's have an average initial particle diameter of 15 µm with a high initial expansion temperature T_s of 208 °C and have their maximum expansion temperature at 249 °C.

2.2. Sample preparation

In this paper, a simple methodology was used to prepare some preliminary foam samples to validate the assumptions of the mathematical model. The microsphere masterbatch and polymer pellets were first dry mixed to prepare a diluted composition of 12 wt% microspheres and 20 wt% glass fibers. The mixture was then fed into a converging twin-screw Haake MiniLab-3 and used to extrude a composite filament at 75 rpm at 180 °C which was later chopped into 10 mm pellets. The composite pellets constitute of 20 wt% glass fibers, 68 wt% PP, and 12 wt% unexpanded

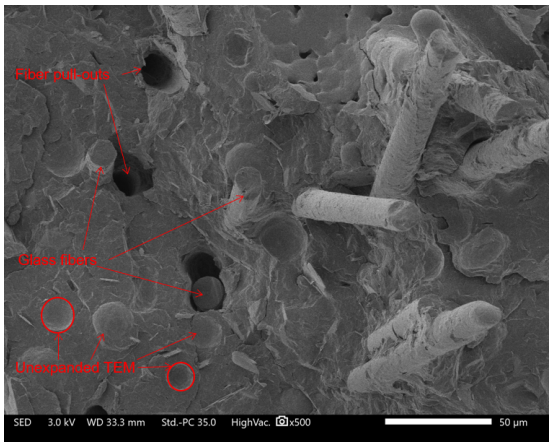

Figure 1. Cross-sectional SEM image of the composite pellet before heat treatment showing unexpanded microspheres and some fibers

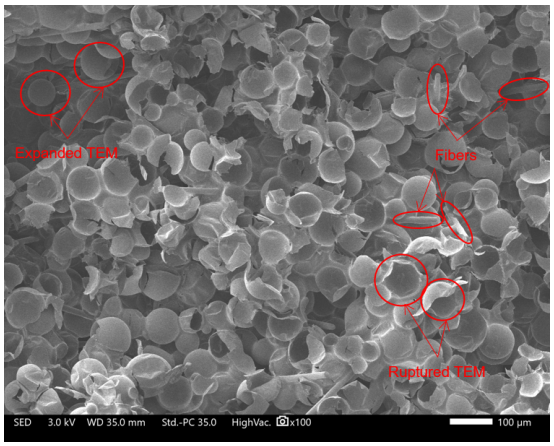

Figure 2. Cross-sectional SEM image of the composite pellet after heat treatment showing expanded microspheres and some fibers

TEM (Fig. 1). Further, these composite pellets were used to prepare the foam samples by heat treatment in an oven for 7 minutes at 240 °C. When the pellets are heated the polymeric shell of the TEM softens and the liquid aliphatic hydrocarbon within the shell vaporises thereby expanding the microsphere and producing the foamed sample (Fig. 2).

2.3. SEM characterization

The microstructure of the two samples was characterized in a scanning electron microscope (SEM) to observe the cell morphology and fiber orientation before and after expansion of the TEM. The samples were prepared using the cryo-fracture technique by immersing the samples in a liquid nitrogen bath for at least 5 minutes and fracturing immediately after removal from the bath. These samples were then sputter-coated with silver before the SEM analysis. The SEM analysis was done under a high vacuum with an acceleration voltage of 3kV, and spatial resolution of $50 - 100$ µm depending on the magnification (x100 to x500).

In the SEM analysis, it was observed that the composite pellet sample compounded with the unexpanded TEM maintained their closed cell spherical geometry with an average diameter of 15 µm (see Fig. 1) even after the composite pellet preparation process. After the heat treatment of the composite samples the TEM rapdily increase in volume as their size increases to an average diameter of 78 µm. In most cases of foam manufacturing processes (other than by using TEM, synthetic hollow rubber, and hollow glass beads) the foam produced are open cell structures which are not spherical in nature and cell sizes are not constant and highly vary depending on the processing parameters [4, 5]. It was verified that although there were few ruptured TEM's observed as an effect of the cryo-fracture, it was evident that the produced foams maintained their closed cell spherical geometry in the fibrous system as well (see Fig. 2).

In the following section, a mathematical model has been developed to investigate the effects of expansion and collapse of a spherical bubble on the fiber suspensions and vice-versa.

3. Mathematical modeling

The mathematical modeling of a gas bubble dynamics in a fiber suspension is now investigated. This problem considers a spherical cavity of radius $R(t)$, whose center O is located at $r = 0$. Due to the symmetry, it is suitable to use the spherical coordinates (r, θ, ϕ), such as the velocity at a point M with a distance r from O is given by $\mathbf{v} = v_r(r,t)\,\mathbf{e}_r$. $\mathbf{e}_r$ represents the unit vector in the outward radial direction at M, as illustrated in Fig. 3. In this configuration, the vorticity tensor is $\Omega = \mathbf{0}$ and the strain rate tensor is given by $\mathbf{D} = \frac{\partial v_r}{\partial r}\mathbf{e}_r\mathbf{e}_r + \frac{v_r}{r}\mathbf{e}_\theta\mathbf{e}_\theta + \frac{v_r}{r}\mathbf{e}_\phi\mathbf{e}_\phi$ (the following notation is used: $2\mathbf{D} = \nabla\mathbf{v} + \nabla\mathbf{v}^\dagger$). Furthermore, it is assumed that the medium surrounding the bubble is incompressible and therefore $\nabla \cdot \mathbf{v} = 0$. From this result, the trace of the strain rate tensor leads to the following equation of continuity

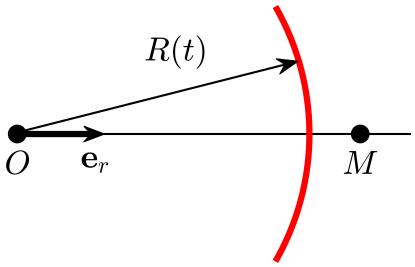

Figure 3. Coordinate systems for the collapsing/expanding bubble problem.

$$\frac{\partial v_r}{\partial r} + 2\frac{v_r}{r} = 0, \tag{1}$$

which gives the solution

$$v_r = \frac{R^2\dot{R}}{r^2}. \tag{2}$$

In the above expression and for clarity, the t-dependency for R has been removed and the upper dot symbol denotes the derivative with respect to time. In the spherical coordinate system, only the radial component is of interest, and therefore the momentum balance equation takes the form

$$\rho\left(\frac{\partial v_r}{\partial t} + v_r\frac{\partial v_r}{\partial r}\right) = -\frac{\partial P}{\partial r} + \frac{\partial \tau_{rr}}{\partial r} + \frac{2\tau_{rr} - \tau_{\theta\theta} - \tau_{\phi\phi}}{r}, \tag{3}$$

where ρ and P refer to the density and the pressure in the surrounding fluid, respectively. The components τ_{ii} ($i = r,\ \theta$ and ϕ) represent the diagonal terms of the extra-stress tensor for the fluid surrounding the bubble. Further, the bubble is presumed to be immersed in a fiber suspension that is considered to be a continuous medium.

3.1. Fiber stress contribution

A general expression for the stress tensor of a suspension made with rigid and cylinder fibers is given by [23, 24, 25]. Using the slender body approximation and the assumption of non-Brownian particles, the constitutive equation can be written as [26, 27, 28, 29]

$$\boldsymbol{\tau} = 2\eta_0\mathbf{D} + 2\eta_0 N_p \mathbf{a_4} : \mathbf{D}. \tag{4}$$

In the above relationship, the suspending fluid displays a Newtonian behavior characterized by the viscosity parameter, η_0. N_p is the particle number [30] and increases with increasing the particle volume fraction, ϕ_f, and the fiber aspect ratio, a_r. Note that the slender fibers assume that $a_r = L/D \gg 1$ that its length, L, is much larger than its diameter, D. Based on these considerations, the parameter N_p, also called the coupling coefficient, measures the degree of how far the fiber suspension behavior differs from the Newtonian one (given by $N_p = 0$). Typical values for N_p can be found in the Dinh and Armstrong theory [28]. $\mathbf{a_4}$ represents the fourth-order orientation tensor [31] and is obtained from the fourth-order moment of ψ, the probability distribution function, such as $\mathbf{a_4} = \int_{\mathbf{p}} \mathbf{pppp}\psi d\mathbf{p}$, where $\mathbf{p}$ is a unit vector directed along the fiber axis. In details, $\int_{\mathbf{p}} ...\psi d\mathbf{p}$ refers to an average over all possible fiber orientations and therefore, $\mathbf{a_4}$ describes the fiber orientation statistics in a representative elementary volume with an efficient and

concise way. The second-order orientation $\mathbf{a_2}$ is commonly used and is defined such as $\mathbf{a_2} = \int_{\mathbf{p}} \mathbf{pp}\psi d\mathbf{p}$. The non-zero components of the extra-stress tensor are found using Eq. (1) and Eq. (4) as

$$\tau_{rr} = -4\eta_0 \frac{v_r}{r} - 2\eta_0 N_p \frac{v_r}{r}\left(2a_{rrrr} - a_{rr\theta\theta} - a_{rr\phi\phi}\right), \tag{5a}$$

$$\tau_{\theta\theta} = 2\eta_0 \frac{v_r}{r} - 2\eta_0 N_p \frac{v_r}{r}\left(2a_{rr\theta\theta} - a_{\theta\theta\theta\theta} - a_{\theta\theta\phi\phi}\right), \tag{5b}$$

$$\tau_{\phi\phi} = 2\eta_0 \frac{v_r}{r} - 2\eta_0 N_p \frac{v_r}{r}\left(2a_{rr\phi\phi} - a_{\theta\theta\phi\phi} - a_{\phi\phi\phi\phi}\right). \tag{5c}$$

The substitution of Eq. (5) into Eq. (3) leads to

$$\rho\left(\frac{\partial v_r}{\partial t} + v_r \frac{\partial v_r}{\partial r}\right) = -\frac{\partial P}{\partial r} - 2\eta_0 N_p \frac{v_r}{r^2}\left(1 - 3a_{rr}\right) + 2\eta_0 N_p \frac{v_r}{r}\frac{\partial}{\partial r}\left(a_{rr} - 3a_{rrrr}\right). \tag{6}$$

Please note that in obtaining the above equation, the r-dependency for orientation tensor components and the fact that $\mathbf{a_4} : \boldsymbol{\delta} = \mathbf{a_2}$ and $\mathbf{a_2} : \boldsymbol{\delta} = 1$ have been taken into account, where $\boldsymbol{\delta}$ is the identity tensor [31]. If Eq. (2) and its corresponding derivatives are substituted in the above relationship, one obtains

$$\frac{2R\dot{R}^2 + R^2\ddot{R}}{r^2} - \frac{2R^4\dot{R}^2}{r^5} = -\frac{1}{\rho}\frac{\partial P}{\partial r} - \frac{2\eta_0 N_p}{\rho}\frac{R^2\dot{R}}{r^4}\left(1 - 3a_{rr}\right) + \frac{2\eta_0 N_p}{\rho}\frac{R^2\dot{R}}{r^3}\frac{\partial}{\partial r}\left(a_{rr} - 3a_{rrrr}\right), \tag{7}$$

Integrating both sides of Eq. (7) with respect to r from r to the infinity gives

$$-\frac{2R\dot{R}^2 + R^2\ddot{R}}{r} + \frac{R^4\dot{R}^2}{2r^4} = -\frac{P - P_\infty}{\rho} + \frac{2\eta_0 N_p}{\rho}\frac{R^2\dot{R}}{3r^3} + \frac{2\eta_0 N_p}{\rho}\int_\infty^r \frac{3R^2\dot{R}}{r^4} a_{rr} dr + \frac{2\eta_0 N_p}{\rho}\int_\infty^r \frac{R^2\dot{R}}{r^3}\frac{\partial}{\partial r}\left(a_{rr} - 3a_{rrrr}\right) dr, \tag{8}$$

where P_∞ is the pressure at a distance far from the bubble center. In this study, all the pressures are absolute pressures.

3.2. Boundary conditions

Let $\sigma_{rr}|_{r=R}$ be the normal stress in the fiber suspension that points radially outward from the center of the microsphere. At some small portion of the bubble surface, the net force per unit area is zero since there is no mass transfer across the boundary. Hence,

$$\sigma_{rr}|_{r=R} + P_{int} - \frac{2T}{R} = 0, \tag{9}$$

where T is the surface tension. Therefore, Eq. (9) becomes

$$P|_{r=R} = P_{int} - 4\eta_0 \frac{\dot{R}}{R} + 2\eta_0 N_p \frac{\dot{R}}{R}\left(a_{rr} - 3a_{rrrr}\right) - \frac{2T}{R}, \tag{10}$$

where P_{int} is the pressure inside the cavity. Upon eliminating the pressure P from Eqs. (8) and (10), the equation describing the time dependence of the bubble radius is found to be

$$R\ddot{R} + \frac{3}{2}\dot{R}^2 + \frac{P_\infty - P_{int}}{\rho} + \frac{2T}{\rho R} + \frac{4\eta_0}{\rho}\frac{\dot{R}}{R} + \frac{2\eta_0 N_p}{\rho}\frac{\dot{R}}{R}\left[\frac{1}{3} + \int_R^\infty \frac{3R^3}{r^4}\left(3a_{rrrr} - 2a_{rr}\right) dr\right] = 0. \tag{11}$$

Let us introduce the bubble radius at the initial instant R_0. By noting that $R = \tilde{R}R_0$ and $t = \tilde{t}\sqrt{\rho R_0^2/P_\infty}$, the dimensionless form of Eq. (11) becomes

$$\tilde{R}\ddot{\tilde{R}} + \frac{3}{2}\dot{\tilde{R}}^2 + 1 - \frac{P_{int}}{P_\infty} + \frac{2}{W_e\tilde{R}} + \frac{4}{R_e}\frac{\dot{\tilde{R}}}{\tilde{R}}\left[1 + \frac{N_p}{2}\left(\frac{1}{3} + I_{\mathbf{a}}\right)\right] = 0, \tag{12}$$

where $W_e = \frac{P_\infty R_0}{T}$ corresponds to the Weber number and $R_e = \frac{\sqrt{\rho R_0^2 P_\infty}}{\eta_0}$ is a Reynolds number. The remaining integrand is defined such as $I_{\mathbf{a}} = \int_{\tilde{R}}^{\infty} \frac{3\tilde{R}^3}{r^4}(3a_{rrrr} - 2a_{rr})\,dr$. Due to the existence of $I_{\mathbf{a}}$ in Eq. (12), the bubble dynamics depends on the fiber orientation and hence on the flow history. When $N_p = 0$, Eq. (12) reduces to the standard equation of bubble dynamics in a Newtonian viscous fluid [32]. When the viscous term is neglected ($R_e \to \infty$), it simplifies to the Rayleigh–Plesset equation [33]. Rayleigh [8] derived a relationship for the collapse time of a spherical cavity of radius R_0 in an infinite fluid with pressure P_∞ and density ρ, considering the time it takes for the fluid to fill the cavity. The derivation is obtained by equating the kinetic energy of the fluid with the work performed by the bubble. This time t_c is defined as

$$t_c = \frac{\Gamma(5/6)}{\Gamma(1/3)}\sqrt{\frac{3\pi}{2}} \approx 0.9147\sqrt{\frac{\rho R_0^2}{P_\infty}}, \tag{13}$$

where $\Gamma(x)$ is the incomplete Gamma function.

3.3. Fiber dynamics

When the fibers are not aligned along the radial streamlines but are initially randomly oriented for instance, the microstructural changes with the flow have to be considered. It is therefore necessary to describe the dynamic behavior of the fiber orientation. An efficient way to represent the fiber orientation distribution is to use the second-order orientation tensor, $\mathbf{a_2}$. The material derivative (D/Dt) of $\mathbf{a_2}$ can be obtained from the expression of $\dot{\mathbf{p}}$ established by Jeffery [34] for ellipsoidal forms in the dilute state. Since fiber interactions may occur in non-dilute suspensions, Folgar and Tucker [35] introduced a randomizing effect of interactions by adding a diffusion term to the Jeffery equation. For slender bodies suspended in a Newtonian fluid, the evolution equation for $\mathbf{a_2}$ is given by

$$\frac{D\mathbf{a_2}}{Dt} = (\Omega\cdot\mathbf{a_2} - \mathbf{a_2}\cdot\Omega) + (\mathbf{D}\cdot\mathbf{a_2} + \mathbf{a_2}\cdot\mathbf{D} - 2\mathbf{a_4}:\mathbf{D}) + 2C_I|D|\,(\delta - 3\mathbf{a_2})\,, \tag{14}$$

where $|D| = \sqrt{2\mathbf{D}:\mathbf{D}}$ is the generalized deformation rate and C_I is the interaction coefficient. If interactions between neighboring fibers are neglected, the interaction coefficient C_I in Eq. (14) is equal to zero and the case of dilute suspensions is recovered. The problem for the fiber dynamics was resolved using a relation called the closure approximation, from which is was possible to express $\mathbf{a_4}$ in term of $\mathbf{a_2}$. The Invariant-Based Optimal Fitting (IBOF) closure [36], which is constructed based on the invariants of $\mathbf{a_2}$, is used in this work. By considering the velocity field encountered until now in the analysis, Eq. (14) reduces to

$$\dot{a}_{rr} + \frac{R^2\dot{R}}{r^2}\frac{\partial a_{rr}}{\partial r} = 6\frac{R^2\dot{R}}{r^3}(a_{rrrr} - a_{rr}) + 4\sqrt{3}C_I\left|\frac{R^2\dot{R}}{r^3}\right|(1 - 3a_{rr}), \tag{15}$$

where $a_{rrrr} = f(a_{rr})$ is obtained from the IBOF closure. The dimensionless form of Eq. (15) is simply obtained by replacing R, $\dot{R}$ and r by $\tilde{R}$, $\dot{\tilde{R}}$ and $\tilde{r}$, respectively.

4. Numerical results

4.1. Bubble collapsing for fixed fiber orientation

As a first approach, the bubble collapse for various steady distributions of fiber orientation was investigated. When the fibers are aligned radially, they remain aligned with the streamlines and $I_{\mathbf{a}} = 1$. On the contrary, when the fibers are in the plane perpendicular to the radial direction, the integrand is found to be $I_{\mathbf{a}} = 0$. Finally a 3D random distribution of fibers leads to $a_{rr} = 1/3$ and $a_{rrrr} = 1/5$ and therefore $I_{\mathbf{a}} = -1/15$. All these values are summarized in Table 1.

Fig. 4 depicts the bubble radius variation with time for a collapsing bubble (i.e., $P_{int} = 0$) in a fiber suspension where the particles are aligned along the radial streamlines (i.e., $I_{\mathbf{a}} = 1$). To obtain these results, the time integration of Eq. (12) is performed by using the Matlab ODE solvers. The accuracy of the numerical method was noted, by indicating a dimensionless collapse time of unity for the simplified Rayleigh-Plesset equation. It can be noticed that the large particle stresses inhibit the collapse of the cavity and can dominate the inertial terms when the radius

Orientation state	$I_{\mathbf{a}}$
Radially aligned	1
Orthoradially aligned	0
3D random	-1/15

Table 1. Integral values for $I_{\mathbf{a}}$ for different fiber orientation distribution

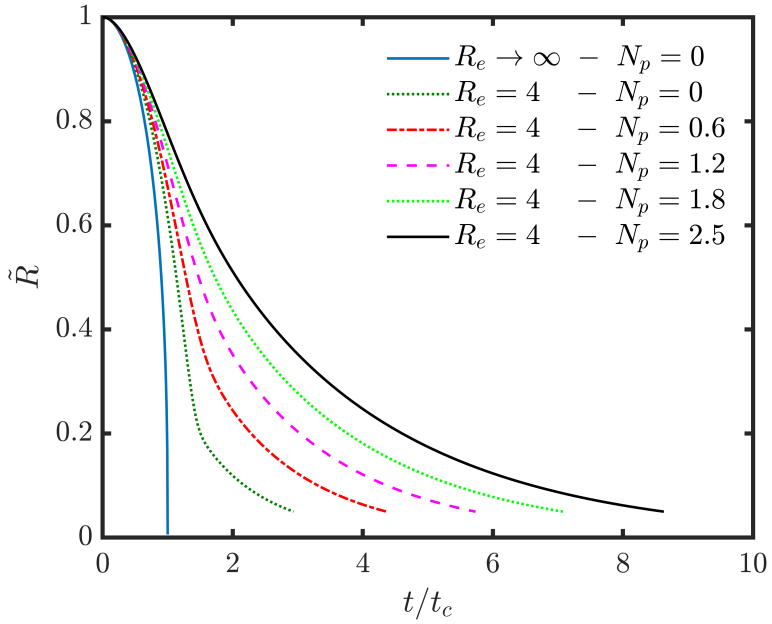

Figure 4. Collapse of a spherical bubble in a fiber suspension where the particles are aligned along the radial streamlines ($I_{\mathbf{a}} = 1$ and $W_e = 0$).

becomes small. The shoulder behaviors observed when the micro-sphere radius becomes small is a result of the very high extensional viscosities when N_p is large, and therefore this mechanism could reduce the bubble damage.

Since the coalescence is slowed down by increasing the viscosity of the surrounding fluid, bubble dynamics in highly viscous fiber suspensions may be of interest to obtain. For low values of Reynolds numbers, viscosity dominates over fluid inertia in retarding the bubble growth. Thus, asymptotic solutions can be recovered from Eq. (12) and result in

$$\tilde{R} = \exp\left\{-\frac{1-\frac{P_{int}}{P_\infty}}{\frac{4}{R_e}\left[1+\frac{N_p}{2}\left(\frac{1}{3}+I_{\mathbf{a}}\right)\right]}\right\}, \tag{16}$$

which are plotted in Fig. 5. It is worth mentioning that inertial effects can be neglected for $N_p > 2.5$ when $R_e = 4$.

4.2. Bubble expanding for fixed fiber orientation

In order to explore the bubble expanding in a fiber suspension under isothermal conditions, the bubble pressure is related to the amount of gas within the bubble at time t according to the ideal gas law, $P_0R_0^3 = PR^3$, where P_0 and P are the pressures inside the bubble at initial time and time t, respectively. To avoid under-pressure in the bubble due to the increase of the radius, the bubble pressure is bounded by the pressure at a distance far from the bubble center. Therefore, one can define the following expression for the pressure inside the bubble

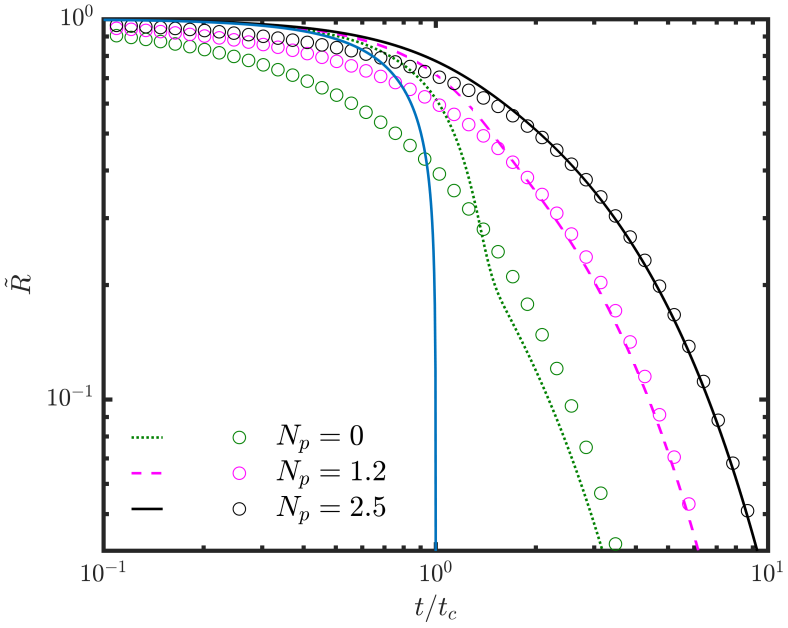

Figure 5. Collapse of a spherical bubble in a fiber suspension when considering inertia (lines) and neglecting inertia (symbols) with $I_{\mathbf{a}} = 1$, $R_e = 4$ and $W_e = 0$. The blue line refers to the blue line in Fig. 4 for which $R_e \to \infty$ and $N_p = 0$.

$$P_{int} = \max\left(P_0 \frac{R_0^3}{R^3}; P_{\text{inf}}\right). \tag{17}$$

When the bubble expands, the steady fiber orientation distribution corresponds to the configuration where all the fibers are orthoradially aligned (i.e., $I_{\mathbf{a}} = 0$). Fig. 6 shows the bubble radius evolution with time. It can be noticed that the bubble radius increases continuously with no viscous contribution (i.e., $R_e \to \infty$), the change of slope coming from the inertial term at short times. When the surrounding fluid is Newtonian (i.e., $R_e = 4$ and $N_p = 0$), the bubble expansion is reduced due to viscous forces. The addition of fibers (i.e., $N_p \neq 0$) further increases viscous forces and therefore reducing the bubble expansion. A steady-state regime can be observed for $R_e = 4$ and $N_p = 2.5$.

The effect of the surface tension have not yet been taken into account. For longer duration, the inertial forces are negligible compared with the viscous and surface tension forces. Hence, the bubble expansion is the result of a competition between these two last forces. Fig. 7 presents the expansion of a spherical bubble in a fiber suspension where the particles remain orthoradially aligned (i.e., $I_{\mathbf{a}} = 0$). It can be noticed that surface tension reduces the final bubble size. For high Weber number, the viscous forces initially dominate during the bubble expansion. Thereafter the influence of the surface tension forces become important leading to reduce the bubble size. By continuing to decrease the Weber number, the characteristic times for the viscous and surface tension forces scale each other and some oscillations for the bubble radius are observed (i.e., $W_e = 10$).

4.3. Bubble expanding with changing fiber orientation

The bubble dynamics in a fiber suspension for which the microstructure can change is governed by Eq. (12) coupled with Eq. (15) through the integrand $I_{\mathbf{a}}$. The problem posed by this set of equations is not so trivial to solve numerically since the movement of the micro-sphere boundary in the suspension must be tracked. Lagrangian coordinates are generally introduced to immobilize the boundary [37] but this approach is not applicable in the present form due to the r dependence of $I_{\mathbf{a}}$. Therefore, the problem is computationally addressed by a finite element discretization carried out in COMSOL Multiphysics with using the arbitrary Lagrangian-Eulerian (ALE) moving mesh method. The global ODEs and DAEs interface is used to implement the ordinary differential equation (ODE) given by Eq. (12) and

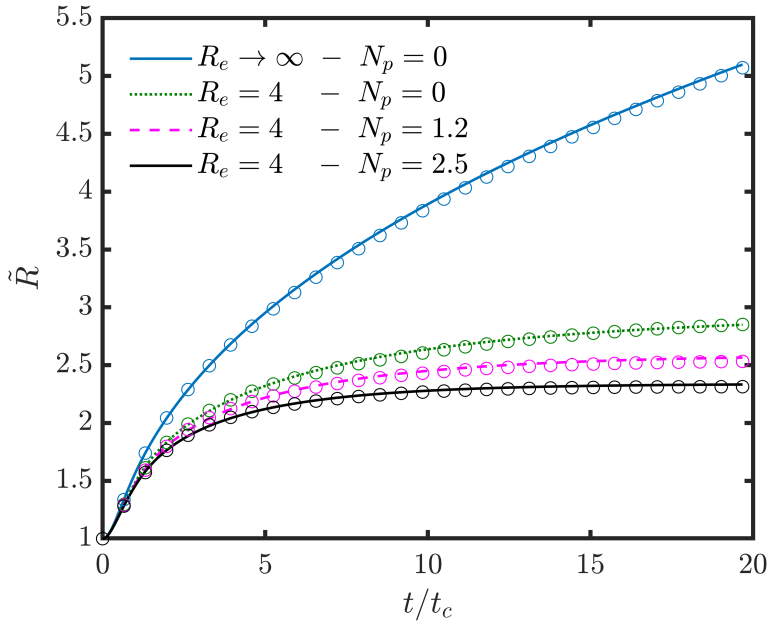

Figure 6. Expansion of a spherical bubble in a fiber suspension where the particles are orthoradially aligned: effects of Reynold number and coupling coefficient ($I_{\mathbf{a}} = 0$, $P_0 = 4$ and $W_e = 0$). Results represented by circles are obtained by solving a coupled ODE-PDE system using COMSOL Multiphysics.

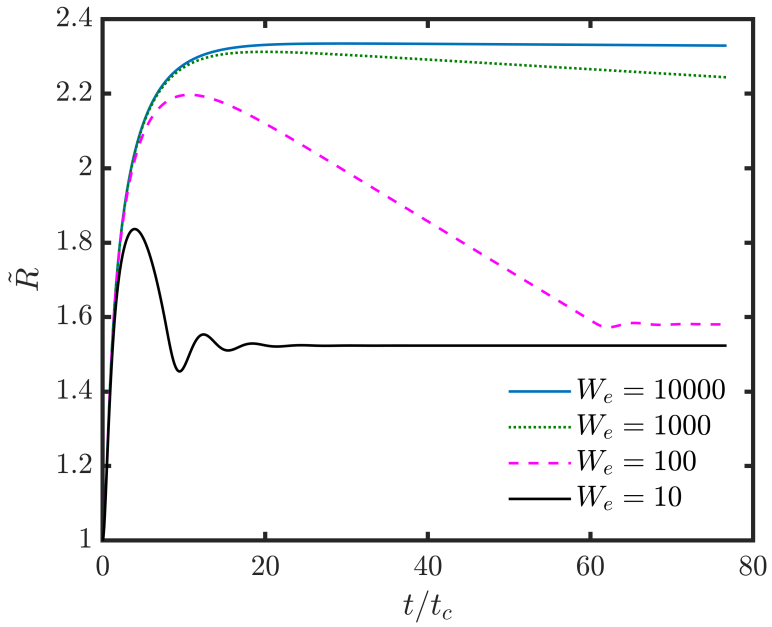

Figure 7. Expansion of a spherical bubble in a fiber suspension where the particles are orthoradially aligned: effect of surface tension ($I_{\mathbf{a}} = 0$, $P_0 = 4$, $R_e = 4$ and $N_p = 2.5$).

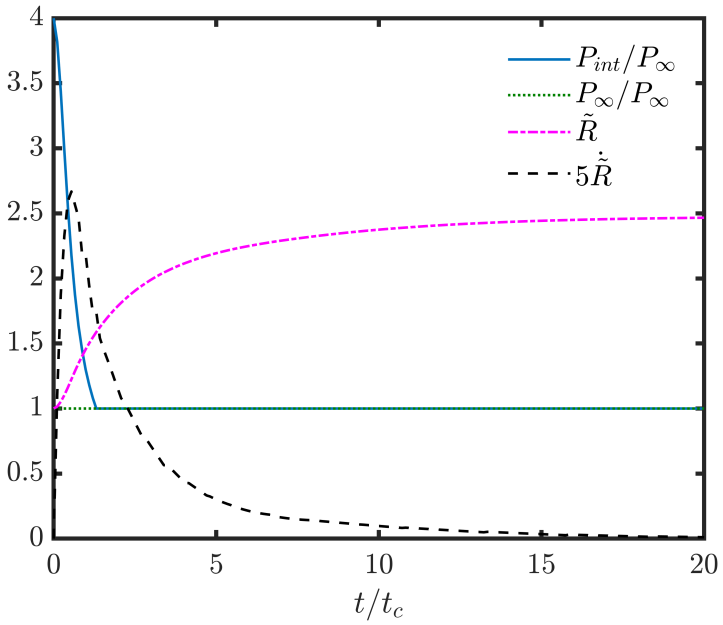

Figure 8. Time evolution of the pressures inside the bubble (P_{int}) and a distance far from the bubble center (P_∞), the bubble radius (R) and its velocity ($\dot{R}$) ($R_e = 4$, $N_p = 2.5$ and $C_I = 0.001$).

the coefficient form PDE interface is used to describe the partial differential equation (PDE) specified by Eq. (15). For the later, the shape function type is Lagrange and the order of finite element is sextic. The 1D mesh consists of 800 elements with an initial size of $150R_0$. This coupled ODE-PDE system is subsequently integrated with the implicit backward differentiation formulas (BDF) method with a prescribed time step of 0.1 s. A domain probe is defined for calculating the integral values of $I_{\mathbf{a}}$. For a fixed fiber orientation where all the particles are aligned in the orthoradial direction (i.e., $a_{rr} = 0$ and $C_I = 0$), the obtained results from this coupled ODE-PDE system are depicted in Fig. 6 for comparison with the previous numerical method. Good accuracy is observed across a range of system parameters and operating conditions.

Now the suspension is considered as an isotropic material with a 3D random fiber orientation distribution (i.e., $a_{rr} = 1/3$). Thus, when the bubble expands because of a higher internal pressure as compared to pressure of the surrounding fluid, it is expected that fiber orientation evolves close to the bubble surface. Fig. 8 depicts these pressures as a function of time. In the time range of 0 to $1.3t/t_c$, the internal bubble pressure remains higher than the pressure far from the cavity, starting with $P_{int} = 4P_\infty$ at $t/t_c = 0$. As previously, the Reynolds number remains unchanged as well as the coupling coefficient and the interaction coefficient is set to $C_I = 0.001$. This force combined with the inertial force increase the bubble radius R until reaching a steady value once the viscous force balances the whole system. The steady-state regime is found to be achieved after $t/t_c > 20$ since the velocity of the bubble radius $\dot{R}$ is close to zero.

Based on this bubble dynamics, the fiber orientation distribution is examined and is reported in Fig. 9. Indeed, the $rr-$components of the second-order orientation tensor are plotted at different time, the latter time corresponds to the quasi-steady-state regime. Only results close to the bubble interface are shown since far from it, i.e. $r/R_0 > 20$, the fiber orientation distribution remains unchanged to the initial and isotropic orientation state (i.e., $a_{rr} = 1/3$). Therefore from $20 < r/R_0 < 150R_0$, a_{rr} is constant and this guarantees the validity of the upper boundary of $I_{\mathbf{a}}$. It can be observed in Fig. 9 that the fibers close to the cavity tend to orient randomly in planes with normal $\mathbf{e}_r$ when the cavity radius increases. Away from the bubble surface, the fibers reach their 3D random orientation since the radial velocity decreases inversely with the square of r (See Eq. 2). For long times (i.e., $t/t_c > 20$), a quasi-steady-state regime is established. Thus, in planes tangent to the bubble surfaces, $a_{\theta\theta} = a_{\phi\phi} = (1 - a_{rr})/2 \approx 0.5$. The biaxial flow

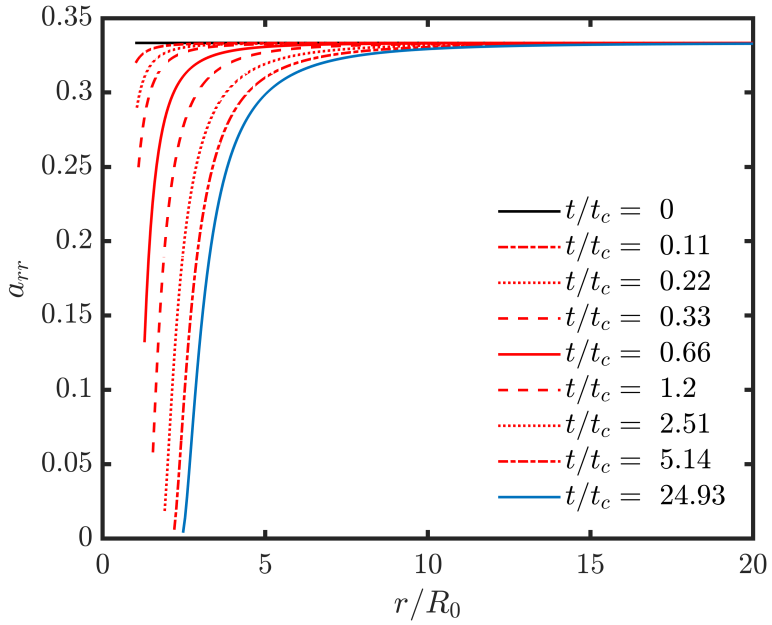

Figure 9. Fiber orientation distribution (a_{rr}) along the $r-$ direction at different times (R_e = 4, N_p = 2.5 and C_I = 0.001).

induces alignment of fibers along the cavity boundaries. It results that the local viscosity will increase leading to avoid the collapse of the bubble, as observed in Fig. 2.

The effect of fiber interactions is presented in Fig. 10 through the variation of the coefficient C_I. The 3D random orientation of the fibers increases, with the increase in interaction coefficient. For dilute fiber suspensions, C_I is close to zero and it can been observed in Fig. 10 that the model will predict that fibers exhibit a 2D random planar orientation in a plane tangent to the bubble surface. Since the viscosity in a biaxial flow depends on the fiber orientation, bubbles will expand more in a suspension where fibers depicts a 3D random orientation than in a suspension where fibers are arranged in a 2D random orientation.

5. Concluding remarks

This study reveals several new and interesting features about gas bubble collapse/expansion in fiber suspensions. The experimental work showed that the TEM maintain their closed-cell spherical geometry throughout the foaming process which was the initial assumption of the mathematical model. To investigate the effects that the fiber orientation changes with the collapse/expansion of the TEM's at a micro-scale level, a system of coupled ODE-PDE has been derived for describing the spherical bubble and the fiber orientation dynamics. Introduction of fiber fillers considerably modifies the bubble dynamics. Among others, fibers prevent bubbles to collapse due to an increase of the elongation viscosity with fiber orientation close to the bubble surface. The proposed approach can be used in further works to consider the intermediate polymeric viscosity of the micro-sphere shell. Thus, the viscoelastic properties of the polymer shell, the evaporation of hydrocarbons in the microsphere and the diffusion behavior of the blowing agent through the polymer shell can also be taken into account. In addition, it is scheduled to develop 2D and 3D numerical models to investigate a bubble growth in a fiber suspension which exhibits micro-structural anisotropies in the polar and azimuthal directions. Another, the future perspective is to stabilize the foaming process and have an in-depth experimental study on the effects of the bubble expansion as a function of time and temperature at a macroscopic scale, and then study the effect of fibers in the foaming process.

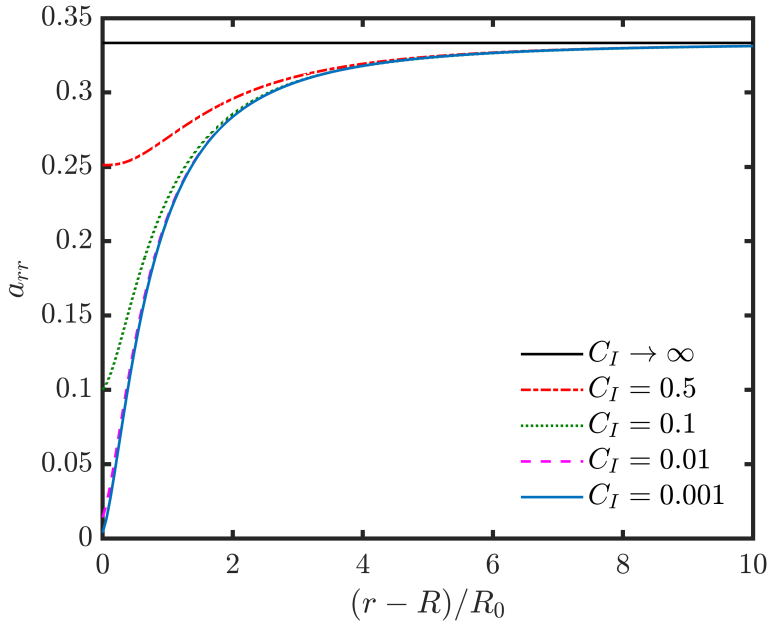

Figure 10. Effect of the fiber interaction coefficient (C_I) on the quasi-steady fiber orientation distribution (a_{rr}) along the $r-$ ($R_e = 4$ and $N_p = 2.5$).

6. Acknowledgments

The first author particularly wishes to acknowledge the Brittany Region for their financial support. The authors would like to acknowledge Kureha GmbH, Germany for supplying thermally expandable microspheres.

References

[1] D. I. Collais, D. G. Baird, Tesile toughness of microcellular foams of polystyrene, styrene-acrylonitrile copolymer, and polycarbonate, and the effect of dissolved gas on the tensile toughness of the same polymer matrices and microcellular foams, Polymer Engineering & Science 35 (14) (1995) 1167–1177. doi:10.1002/pen.760351407.

[2] J. Wang, H. Xie, Z. Weng, T. Senthil, L. Wu, A novel approach to improve mechanical properties of parts fabricated by fused deposition modeling, Materials and Design 105 (2016) 152–159. doi:10.1016/j.matdes.2016.05.078.

[3] J. N. Yang, G. X. Ding, Z. F. Wang, J. S. Gao, Fabrication and characterization of short glass fiber reinforced polypropylene hybrid composite foams, Journal of Reinforced Plastics and Composites 34 (22) (2015) 1871–1883. doi:10.1177/0731684415602071.

[4] C. Wang, S. Ying, Batch foaming of short carbon fiber reinforced polypropylene composites, Fibers and Polymers 14 (5) (2013) 815–821. doi:10.1007/s12221-013-0815-y.

[5] S. P. Xiao, H. X. Huang, Generation of nanocellular TPU/reduced graphene oxide nanocomposite foams with high cell density by manipulating viscoelasticity, Polymer 183 (2019) 121879. doi:10.1016/j.polymer.2019.121879.

[6] G. Petrossian, C. J. Hohimer, A. Ameli, Highly-loaded thermoplastic polyurethane/lead zirconate titanate composite foams with low permittivity fabricated using expandable microspheres, Polymers 11 (2) (2019). doi:10.3390/polym11020280.

[7] S.-P. Wang, A.-M. Zhang, Y.-L. Liu, S. Zhang, P. Cui, Bubble dynamics and its applications, Journal of Hydrodynamics 30 (6) (2018) 975–991. doi:10.1007/s42241-018-0141-3.

[8] O. Lord Rayleigh, III On the pressure developed in a liquid during the collapse of a spherical cavity, The London, Edinburgh, and Dublin Philosophical Magazine and Journal of Science 34 (200) (1917) 94–98. doi:10.1080/14786440808635681.

[9] M. S. Plesset, P. Calif, The dynamics of cavitation bubbles, ASME Journal of Applied Mechanics 16 (1949) 228–231.

[10] M. S. Plesset, A. Prosperetti, Bubble dynamics and cavitation, Annual Review of Fluid Mechanics 9 (1977) 145–185. doi:10.1146/annurev.fl.09.010177.001045.

[11] J. R. Street, A. L. Fricke, L. P. Reiss, Dynamics of phase growth in viscous, non-newtonian liquids. initial stages of growth, Industrial & Engineering Chemistry Fundamentals 10 (1) (1971) 54–64. doi:10.1021/i160037a011.

[12] A. Arefmanesh, S. G. Advani, Diffusion-induced growth of a gas bubble in a viscoelastic fluid, Rheologica Acta 30 (3) (1991) 274–283. doi:10.1007/BF00366641.

[13] A. Arefmanesh, S. G. Advani, Nonisothermal bubble growth in polymeric foams, Polymer Engineering & Science 35 (3) (1995) 252–260. doi:10.1002/pen.760350306.

[14] J. S. Allen, R. A. Roy, Dynamics of gas bubbles in viscoelastic fluids. i. linear viscoelasticity, The Journal of the Acoustical Society of America 107 (6) (2000) 3167–3178. doi:10.1121/1.429344.
[15] J. S. Allen, R. A. Roy, Dynamics of gas bubbles in viscoelastic fluids. ii. nonlinear viscoelasticity, The Journal of the Acoustical Society of America 108 (4) (2000) 1640–1650. doi:10.1121/1.1289361.
[16] Y. Kawaguchi, M. Ohshima, M. Tanida, T. Ohishi, A. Ito, T. Sawa, Development of thermally expandable microcapsule and their mathematical models for polymer foaming, Seikei-Kakou 23 (10) (2011) 627–635. doi:10.4325/seikeikakou.23.627.
[17] M. Fujino, T. Taniguchi, Y. Kawaguchi, M. Ohshima, Mathematical models and numerical simulations of a thermally expandable microballoon for plastic foaming, Chemical Engineering Science 104 (2013) 220–227. doi:10.1016/j.ces.2013.09.010.
[18] B. E. Verweyst, C. L. Tucker, Fiber suspensions in complex geometries: Flow/Orientation coupling, The Canadian Journal of Chemical Engineering 80 (6) (2002) 1093–1106. doi:10.1002/cjce.5450800611.
[19] D. Mezi, G. Ausias, Y. Grohens, J. Férec, Numerical simulation and modeling of the die swell for fiber suspension flows, Journal of Non-Newtonian Fluid Mechanics 274 (2019) 104205. doi:10.1016/j.jnnfm.2019.104205.
[20] D. Mezi, G. Ausias, S. G. Advani, J. Férec, Fiber suspension in 2d nonhomogeneous flow: The effects of flow/fiber coupling for newtonian and power-law suspending fluids, Journal of Rheology 63 (3) (2019) 405–418. doi:10.1122/1.5081016.
[21] J. G. Evans, The flow of a suspension of force-free rigid rods in a Newtonian fluid, Ph.D. thesis, University of Cambridge, Cambridge, UK (1975).
[22] J. G. Evans, The effect of the non-newtonian properties of a suspension of rod-like particles on flow fields, in: J. Hutton, K. W. Pearson (Eds.), Theoretical Rheology, Applied Science Publishers, London, 1975, Ch. 14, pp. 224–232.
[23] E. J. Hinch, L. G. Leal, Constitutive equations in suspension mechanics. part 1. general formulation, Journal of Fluid Mechanics 71 (3) (1975) 481–495. doi:10.1017/S0022112075002698.
[24] E. J. Hinch, L. G. Leal, Constitutive equations in suspension mechanics. part 2. approximate forms for a suspension of rigid particles affected by brownian rotations, Journal of Fluid Mechanics 76 (1) (1976) 187–208. doi:10.1017/S0022112076003200.
[25] G. G. Lipscomb, M. M. Denn, D. U. Hur, D. V. Boger, The flow of fiber suspensions in complex geometries, Journal of Non-Newtonian Fluid Mechanics 26 (3) (1988) 297–325. doi:10.1016/0377-0257(88)80023-5.
[26] G. K. Batchelor, The stress system in a suspension of force-free particles, Journal of Fluid Mechanics 41 (3) (1970) 545–570. doi:10.1017/S0022112070000745.
[27] G. K. Batchelor, The stress generated in a non-dilute suspension of elongated particles by pure straining motion, Journal of Fluid Mechanics 46 (4) (1971) 813–829. doi:10.1017/S0022112071000879.
[28] S. M. Dinh, R. C. Armstrong, A rheological equation of state for semiconcentrated fiber suspensions, Journal of Rheology 28 (3) (1984) 207–227. doi:10.1122/1.549748.
[29] J. Férec, E. Bertevas, B.-C. Khoo, G. Ausias, N. Phan-Thien, The effect of shear-thinning behaviour on rod orientation in filled fluids, Journal of Fluid Mechanics 798 (1) (2016) 350–370. doi:10.1017/jfm.2016.323.
[30] C. L. Tucker, Flow regimes for fiber suspensions in narrow gaps, Journal of Non-Newtonian Fluid Mechanics 39 (3) (1991) 239–268. doi:10.1016/0377-0257(91)80017-E.
[31] S. G. Advani, C. L. Tucker, The use of tensors to describe and predict fiber orientation in short fiber composites, Journal of Rheology 31 (8) (1987) 751–784. doi:10.1122/1.549945.
[32] W.-J. Yang, H.-C. Yeh, Theoretical study of bubble dynamics in purely viscous fluids, AIChE Journal 12 (5) (1966) 927–931. doi:10.1002/aic.690120517.
[33] H. Lin, B. D. Storey, A. J. Szeri, Inertially driven inhomogeneities in violently collapsing bubbles: the validity of the rayleigh–plesset equation, Journal of Fluid Mechanics 452 (2002) 145–162. doi:10.1017/S0022112001006693.
[34] G. Jeffery, The motion of ellipsoidal particles immersed in a viscous fluid, Proceedings of the Royal Society of London 102 (1922) 161–179. doi:10.1098/rspa.1922.0078.
[35] F. Folgar, C. L. Tucker, Orientation behavior of fibers in concentrated suspensions, Journal of Reinforced Plastics and Composites 3 (2) (1984) 98–119. doi:10.1177/073168448400300201.
[36] D. H. Chung, T. H. Kwon, Invariant-based optimal fitting closure approximation for the numerical prediction of flow-induced fiber orientation, Journal of Rheology 46 (1) (2002) 169–194. doi:10.1122/1.1423312.
[37] A. Aliabadi, A. Taklifi, The effect of magnetic field on dynamics of gas bubbles in visco-elastic fluids, Applied Mathematical Modelling 36 (6) (2012) 2567–2577. doi:/10.1016/j.apm.2011.09.040.